In situ investigation of annealing effect on thermophysical properties of single carbon nanocoil

Chenghao Deng [a,c], Tianze Cong [b], Yangsu Xie [c], Ridong Wang [c], Tianyu Wang [c], Lujun Pan [b], Xinwei Wang [c,*]

[a] Center on Nanoenergy Research, School of Physical Science and Technology, Guangxi University, Nanning 530004, PR China
[b] School of Physics, Dalian University of Technology, No. 2 Linggong Road, Ganjingzi District, Dalian 116024, PR China
[c] Department of Mechanical Engineering, Iowa State University, 271 Applied Science Complex II, Ames, IA 50011, USA

A B S T R A C T

In reported high-temperature annealing of carbon nanocoils (CNCs), the samples studied before and after annealing are different ones. This significantly hinders annealing effect understanding due to unknown and remarkable sample-to-sample structure difference. Here using the transient electro-thermal technique (TET) and current-induced annealing, we report the first time in situ investigation of annealing effect on the thermophysical properties for the same individual CNC. Our dynamic annealing track uncovers an electrical resistance relation with annealing time as $R \sim -R_s \ln(t)$. The reaction rate (R_s) shows a normal distribution against the annealing power/temperature, proposing that the activation energy for structure reconstruction in CNCs follows a normal distribution. After annealing at 5–35€μA, the average thermal diffusivity (α) and electrical conductivity (σ) of CNCs show respective 50–160% and 100–170% increase. Normative linear relation between α and σ is discovered, which proposes axial-direction parallel structure in CNCs. The nonuniform temperature distribution along the sample during annealing creates different annealing levels and provides a great advantage to study the relation between structure and thermophysical properties. Our micro-scale Raman characterization reveals the nonuniform distribution of grain size along the length direction of CNCs after annealing and finds a rapid grain size increase from 4.0 to 7.8 nm near the sample's middle point. The middle point of the sample has the highest temperature rise (T_c), largest thermal conductivity (κ) increase, and the most dramatic structure improvement. Its κ shows a rapid improvement (8.7-fold maximum change) from 1200 K to 1800 K. A linear relation between κ^{-1} and T_c is observed and is attributed to the change of grain size during annealing. Using the concept of thermal reffusivity $(\Theta=1/\alpha)$, a 1-fold increase of average grain size and a 197 K decrease of Debye temperature of CNCs after annealing are uncovered.

1. Introduction

Among carbon nanomaterials family, there is a representative quasi 1-dimensional material with unique helix morphology, called carbon nanocoil (CNC) [1-6]. The helical geometry of CNCs distinguishes them from carbon nanotubes (CNTs) and carbon nanofibers (CNFs), vesting them distinct advantages in mechanical [7,8] and electromagnetic properties [9,10]. CNCs have potential applications in wearable sensors [11-14], micro/nano electromechanical systems [15,16], field emitters [17,18], electrochemical devices [19,20], wave absorption [21,22], templates for nanomaterials synthesis [23,24] and so on.

Special morphology always corresponds to special internal structure. Different from the perfect graphite structure of CNTs and disordered structure of amorphous carbon, the polycrystalline-amorphous structure of CNCs exhibits special effect on their physical properties [25-27]. CNCs' sp^2 grains are embedded in their amorphous carbon networks [7]. These sp^2 grains act like nanoparticles and hop electrons from one grain to another, overcoming certain barriers. Amorphous carbon networks are like insulative media, blocking/reducing the transport of electrons and phonons. They also work as spinning sites, impeding the propagation of slide of sp^2 grains and graphite layers under stress, which improves the mechanical strength of CNCs [28]. High-temperature annealing has been employed to improve the graphitization degree of CNCs. It

* Corresponding author.
E-mail address: xwang3@iastate.edu (X. Wang).

was found that even highly oriented CNCs annealed at 2873 K still have a great number of unrepaired defects [29]. In simulation models, the formation of CNCs is a result of periodically inserting pairs of five-fold rings and seven-fold rings into homogeneous six-fold rings of CNTs [30] .Even if CNCs have perfect crystal structure, they are different from CNTs.

The annealing effect on electrical and mechanical properties of CNCs has been well investigated. Different electron hopping mechanisms at different temperatures were proposed [25,31]. It was found that larger grain size leads to smaller hopping energy for electron transport [29]. Using high-temperature annealing in a furnace, the relationship between electrical properties and internal structures of CNCs were studied [29]. With annealing temperature increased from 973 to 2473 K, the average grain size of CNCs increases from 4 to 14 nm, its electrical resistivity decreases from 1.9×10^{-4} to 3.5×10^{-5} Ω m and the average activation energy for electron hopping decreases from 11 to 4.2 meV. However, even though CNCs were annealed at temperatures up to 2873 K, the resistivity of CNCs was still higher than that of some multiwalled CNTs [32]. This may originate from different electrical conductance mechanism between CNTs and CNCs. Also a great number of unrepaired defects in annealed CNCs contribute to their poor resistivity. The mechanical strength of CNCs was found to be determined by graphite grains slide [28,33]. High temperature annealing experiments in a graphite furnace revealed the non-linear annealing effect on correlation between crystallinity and oscillation of CNCs [34]. Two types of energy dissipation were proposed, which are structural anomalies for less crystalline CNCs and interlayer slipping for higher crystalline CNCs.

In the past, we have measured the average room temperature (RT) thermal conductivity (κ) of as-grown CNCs to be 3 W/m K using a transient electro-thermal (TET) technique [35]. Through radiation spectrum, Ma et al. measured the κ of a single CNC during the process of field emission to be 38 W/m K, which corresponds to a high annealing temperature up to 2000 K [36]. High temperature annealing shows remarkable effect on thermal properties of CNCs. Considering the special polycrystalline-amorphous structure of CNCs, it is of great importance to understand how the crystallinity of CNCs affects their thermal properties. Aforementioned annealing effect research targeting electrical and mechanical properties were relied on furnace heating, which were hindered by sample-to-sample structure variation and were very cumbersome. Besides furnace heating, current-induced annealing has also been used for improving the crystallinity of nanomaterials. Benefitting from the same device structure for TET characterization and Joule heating annealing, we are able to complete the in situ annealing and thermophysical characterization of a same single CNC sample. This promotes much higher-level understanding of the annealing effect on structure and thermal transport properties. In this paper, individual CNCs were subjected to high-current induced Joule heating annealing. The RT thermal diffusivity (α) and electrical conductivity (σ) of CNCs after different-level annealing were measured in situ using the TET technique. The correlation among thermal properties, graphite grain size and annealing temperature were investigated systematically.

2. Experimental

2.1. Sample preparation

CNCs were synthesized at 710 °C by using a chemical vapor deposition (CVD) method with the assistance of Fe-Sn composite catalysts using C_2H_2 as carbon source [37]. Then individual CNCs were extracted from as-grown CNC clusters and were then suspended between two electrodes using silver paste, with the help of micromanipulators and microprobes. The two-electrode micro de-
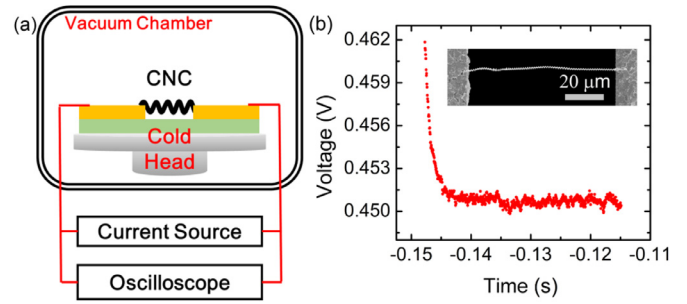

Fig. 1. (a) Schematic for TET characterization and current induced thermal annealing. (b) Typical voltage evolution of a CNC sample (sample 1) during TET characterization. The total length of sample 1 (considering helical morphology) is 132 μm. The inset in (b) is the SEM image of the suspended CNC sample.

vice consists of two separated iridium electrodes fixed on a glass substrate, with 40–80 μm gap between them. The electrodes were prepared by sputtering 100 nm thick iridium films on glass flakes. Schematic and scanning electron microscope (SEM) image of individual CNC device are shown in Fig. 1(a) and (b) respectively.

2.2. TET characterization

As schematically illustrated in Fig. 1(a), an individual CNC device is housed in a vacuum chamber, with pressure less than 1 Pa. The α of individual CNCs was measured by using the TET method [38]. In TET measurement, a step current generated by a current source, ranging from 0.2–2 μA, was fed into the individual CNC. Originating from negative resistance-temperature coefficient, the resistance of CNCs decreases under Joule heating, presenting a voltage evolution recorded by an oscilloscope. A voltage evolution curve of a typical CNC sample (sample 1) is shown in Fig. 1(b). This voltage evolution is determined by two competitive processes: heating by the electrical current, and heat conduction along the sample to the electrode. From the voltage evolution curve, the α of an individual CNC can be determined by fitting it using a developed physical model that relates the normalized voltage evolution to sample's α. The heat conduction in CNC samples can be regarded as 1D thermal transport during TET characterization. The governing equation is expressed as [39]

$$\frac{\partial(\rho c_p T)}{\partial t} = \kappa \frac{\partial^2 T(x)}{\partial x^2} + \frac{I^2 R}{AL} - \frac{4\varepsilon\sigma_B(T^4 - T_0^4)}{d}, \quad (1)$$

where R, A, L, d, κ and ρc_p are coil's electrical resistance, cross sectional area, length, diameter, thermal conductivity and specific heat. RT c_p of CNCs has been measured to be 910 J/kg K [35]. I is the current fed through the sample. The item $4\varepsilon\sigma_B(T^4 - T_0^4)/d$ describes the effect of thermal radiation, where ε (=0.85) is surface emissivity, σ_B is the Stefan-Boltzmann constant. The normalized voltage (V^*) evolution is proportional to temperature rise, and is related to the sample's α as [40]:

$$V^* = (V - V_0)/(V_\infty - V_0)$$
$$= \frac{96}{\pi} \sum_{m=1}^{\infty} \frac{1 - \exp(-(2m-1)^2\pi^2\alpha_{eff}t/L^2)}{(2m-1)^4}. \quad (2)$$

V_0 and V_∞ are the initial and final state voltage, and α_{eff} is the effective α that includes the radiation effect. The sample's intrinsic α can be calculated as $\alpha = \alpha_{eff} - 16\varepsilon\sigma_B T^3 L^2/\pi^2 d\rho c_p$. Detailed principles of sample preparation and TET characterization can be found in our previous work [35].

2.3. Annealing of individual CNCs using Joule heating

To address the effect of structure on thermal properties of CNCs, current induced thermal annealing in a vacuum chamber was car-
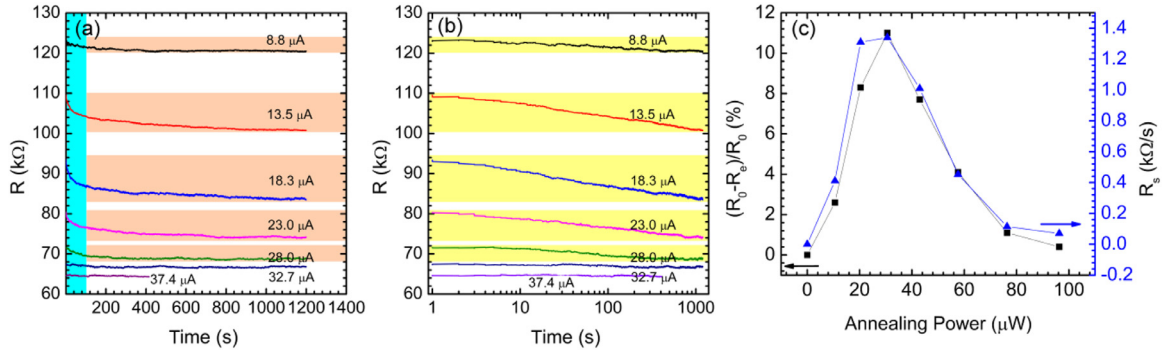
Fig. 2. (a) Resistance evolution curves under different annealing current for sample 1. (b) Log-vision of resistance evolution. (c) Variation of relative resistance change (δR) and resistance changing speed (R_s) with increased annealing power for sample 1.

ried out. As shown in Fig. 1(a), in the vacuum chamber, 5–35 μA current was applied to anneal individual CNCs through Joule heating. Resistance evolution during the annealing process was monitored by an oscilloscope. The annealing lasted for 20 min till the resistance became almost stable. RT α and σ of the same CNC sample were measured after annealing at each current. Low temperature TET tests from 290 to 10 K for CNC samples before and after annealing were carried out to investigate the annealing effect on low temperature thermal behavior and grain size.

3. Results and discussion

3.1. Dynamic structure evolution and electron transport change by annealing

The evolution of electrical resistance during annealing was first characterized and investigated. Fig. 2(a) shows the resistance evolution of sample 1 under different annealing currents. Every annealing process lasts for 20 min, and then the annealing current is changed to a higher level. It is found that the resistance decreases rapidly in the first 100 s of each annealing process. Defining R_0 and R_e as initial and final resistance of the annealing process, the relative resistance change (δR) is expressed as $(R_0 - R_e)/R_0 \times 100\%$ and is used to characterize the process. It is worth noting that R_e of each annealing process (hot ending point) is larger than R_0 of next annealing process (cold starting), which is attributed to the negative resistance-temperature coefficient of CNCs. Governed by the thermal transport process, the annealing temperature is proportional to the annealing power. Here we use Joule thermal power ($I^2 R_e$) to describe the effect of annealing temperature on resistance of CNCs. Fig. 2(c) presents δR under different annealing power. δR increases with increased annealing power until 30 μW, then it goes down. To shed more light on the resistance change in the first 100 s, we take the log-vision of time, as shown in Fig. 2(b). It is found that the resistance evolution ($t > 4$ s) can be well fitted as

$$R = R_0 - R_s \ln(t). \tag{3}$$

The changing rate of resistance during annealing is given as $dR/dt = -R_s/t$, which decreases with annealing time. With annealing proceeding (t increasing), the improved crystallinity and decreased electrical resistance under Joule heating are becoming saturated.

Within the first 4 s of annealing time, the changing rate of resistance is much smaller than that of the region of $t > 4$ s. Annealing is the reconstruction of covalent bonds. In the annealing time of the first 4 s, there may be some other physical processes (like the rotation of sp^2 grains or the thermal expansion of sp^2 grains) and reconstruction of bonds may have not started yet. As a proportional constant, R_s reflects the changing speed of resistance, which shows very similar variation trend to δR with increased annealing

power [Fig. 2(c)]. Although the crystallinity of CNCs improves with increased annealing temperature, the resistance does not change linearly with crystallinity improvement. Ma et al. have reported the annealing effect on electrical properties of CNCs achieved by high-temperature furnace. It was uncovered that the electrical resistivity of CNCs decreases sharply from 1.9×10^{-4} to 7.7×10^{-5} Ω€m when the annealing temperature is increased from 973 to 1073 K, then it is around 7.1×10^{-5} Ω€m in the temperature range of 1273 to 2473 K. This phenomenon accounts for the largest δR at 30 μW and the gradual reduction of δR in the stage of 30–96 μW in our work. δR at 96 μW becomes almost zero. From another point of view, with increased annealing power, the temperature is more determined by radiation heat loss, resulting in more uniform temperature distribution along the length direction of the sample and a limited temperature increase for further annealing. It is worth noting that, the value of R_s and δR are influenced by the annealing history. When a high current (30–50 μA) is fed into a virgin CNC sample directly, larger R_s and δR will be observed. The normal distribution of R_s and δR with annealing power indicates that the activation energy for structure reconstruction may follow a normal distribution.

3.2. Correlation between electron and heat conduction

Fig. 3(a) shows the RT σ and α measured using the TET technique for sample 1 [shown in Fig. 3(b)] after annealing at different annealing power. With annealing power increased from 0 to 76 μW, the σ and α of increase from 1.37×10^4 to 2.74×10^4 S/m and from 1.48×10^{-6} to 2.23×10^{-6} m^2/s, respectively. They are improved by 100% and 51% respectively. Both of them show rapid increase in the power range of 20 to 40 μW. Under a given electrical current, the heating effect induced by the current will be affected by the cross-sectional area of CNC samples, which leads to the difference among samples. To figure out this difference, we employ power areal density and normalized change of α ($\delta\alpha$) and σ ($\delta\sigma$) with respect to their original values. Power areal density is equal to the ratio of Joule heating power to cross-sectional area of CNCs. Fig. 3(c) shows the normalized $\delta\alpha$ and $\delta\alpha$ under different power areal density of two CNC samples (sample 1 and 2). The four parameters follow the similar variation trend. The total length (L) and fiber diameter (d) of the two CNC samples are 132 μm and 259 nm, 99 μm and 301 nm, respectively, which are marked in Fig. 3(b). Using a fitting and differential method, it is found that the σ and α of the two samples change fastest at the power density of 480×10^6 W/m^2. This is expectable due to the normal distribution of activation energy uncovered in Fig. 2(c).

The σ and α show almost identical variation trend with increased annealing power, as depicted in Fig. 3(a). Their relation is further studied by directly comparing the change of α and
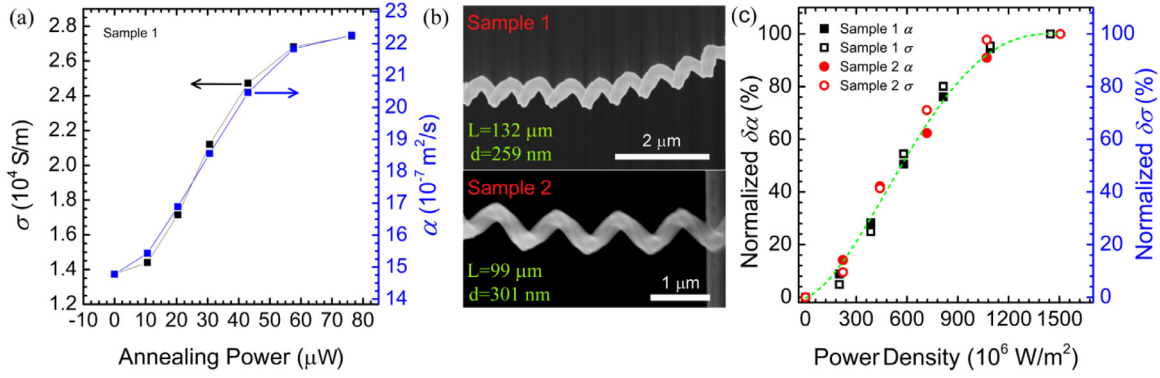
Fig. 3. (a) Variation of α and σ with increased annealing power. (b) Enlarged SEM images of samples 1 and 2. (c) Correlation between normalized change of α and σ versus annealing power areal density of the two CNC samples.
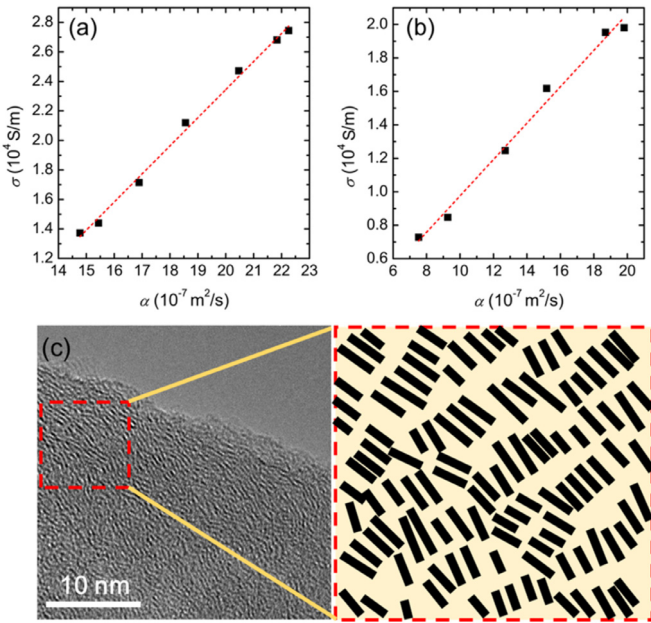

Fig. 4. Linear relationship between σ and α of two CNC samples: (a) for sample 1 and (b) for sample 2. (c) High resolution TEM image of a typical CNC and schematic representation for the internal structure of CNCs.

σ. Figs. 4(a) and (b) uncover a linear relation between σ and α of sample 1 and 2. This linear relation is quite similar to the Wiedemann-Franz law, but should be explained using different physics. The Wiedemann-Franz law describes the relationship between thermal conductivity (κ) and electrical conductivity (σ) of metal materials: $\kappa/\sigma = L_z T$, where L_z is Lorentz constant with a value of 2.44×10^{-8} W Ω/K^2. Using the average σ (2.06×10^4 S/m) in Fig. 4(a) and temperature of 300 K, we estimate the electron thermal conductivity to be 0.15 W/m K. The overall thermal conductivity is estimated as the product of average α (18.5×10^{-7} m^2/s) and RT specific heat (910 J/kg K) of CNCs measured in our previous work [35], getting 3.7 W/m K as a result. The contribution of electron thermal transport to overall thermal conductivity is less than 5%, which is negligible as a consequence. Thus, we consider the linear relation between σ and α is not governed by the physics of Wiedemann-Franz law but originates from internal structure.

To address this issue, a high resolution transmission electron microscope (TEM) image of CNCs is presented in Fig. 4(c), where the polycrystalline-amorphous structure can be observed. sp^2 grains are embedded in sp^3 amorphous networks. The elec-

trical and thermal transports of metals are all governed by free electrons, determining the proportional relation between σ and κ. For CNCs, the electron and phonon transports are all localized by graphite nanograins and the amorphous networks between them. On this account, hopping conduction mechanism for electron transport has been proposed [29]. Electron transport is impeded by hopping barrier between graphite nanograins. Like electrons, we can define a phonon barrier for phonon transportation between nanograins. The κ of sp^2 structured carbon can reach 300–3000 W/m K, while that of amorphous carbon is always less than 0.5 W/m K [41]. The huge κ difference between these two different structures prompts a barrier when phonons transport between two adjacent sp^2 nanograins. That is, both electron and phonon transports are more controlled by the size of sp^2 grains and the amorphous carbon gap between them.

Here we define the α and σ of sp^2 grains as α_a and σ_a, while those of amorphous carbon are α_b and σ_b. sp^2 grains are layered structures and show anisotropic σ and α within the layer and between the layers. Using TEM and electron diffraction, the (002) lattice plane of sp^2 grains has been discovered almost parallel to the coil axis [34], also can be observed from Fig. 4(c). When the sp^2 grains are aligned, it is reasonable to express the α (σ) of CNCs as a linear combination of the α (σ) of sp^2 grains and amorphous carbon [42] as:

$$\begin{aligned} \alpha &= \gamma\alpha_a + (1-\gamma)\alpha_b \\ \sigma &= \gamma\sigma_a + (1-\gamma)\sigma_b \end{aligned} \tag{4}$$

where γ is the volume fraction of sp^2 grains of a CNC. High-temperature annealing will increase the value of γ. From Eq. (4) we get $\sigma = k(\alpha - \alpha_b) + \sigma_b$, where $k = (\sigma_a - \sigma_b)/(\alpha_a - \alpha_b)$. sp^3 amorphous carbon can be treated as insulating material whose σ (σ_b) is almost zero. But the α (α_b) is still non-trivial. Then we have $\sigma = k(\alpha - \alpha_b)$. The two curves in Fig. 4(a) and (b) can be fitted using this function, expressed as:

$$\sigma_1 = 0.19(\alpha_1 - 5.7), \qquad \sigma_2 = 0.11(\alpha_2 - 1.0), \tag{5}$$

where the units of σ and α are 10^4 S/m and 10^{-7} m^2/s respectively. The difference of k comes from the structural difference of the two samples. The maximum changes of σ and α of sample 2 after annealing are 172% and 163%. Compared to sample 1, sample 2 has a larger fiber diameter and resulting poorer crystallinity. This result indicates that the α and σ of less crystalline CNCs are more sensitive to crystallinity improvement during the annealing process, and reversely for more crystalline CNCs. Combining the results of the two samples, it is found that σ shows greater improvement than α after annealing. Considering a limit case, the α of the two samples become 5.7×10^{-7} and 1.0×10^{-7} m^2/s when their σ reaches zero, which correspond to the residual α
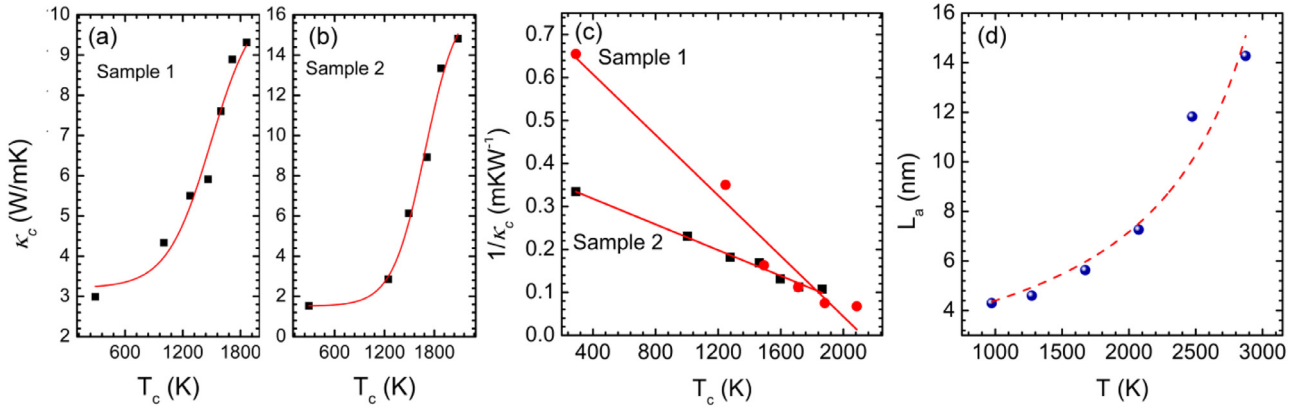
Fig. 5. (a) and (b) Localized κ of the middle point (κ_c) for the two CNC samples after being annealed at different temperatures. (c) Linear relation between $1/\kappa_c$ and T_c.(d) Variation of sp^2 grain size (L_a) with increased annealing temperature from the work of Ma et al. [29] (reproduced with permission).

when the sample becomes an insulative material just like amorphous carbon. Using the measured specific heat of CNCs in our previous work (910 J/kg K) [35], the limit thermal conductivities of the two samples are 1.1 W/m K and 0.2 W/m K, which are close to that of amorphous carbon [43]. Considering the electrical contact resistance between CNC and electrodes, the measured σ is expected to be smaller than its real value. When the contact resistance is reduced, the linear curves in Fig. 4(a) and (b) will shift upwards along the vertical axis, resulting in a decreased α limit.

3.3. Effect of nonuniform temperature distribution along CNC

In our annealing process, the sample has nonuniform temperature rise: highest in the middle and lowest at the ends that are contacted with the electrodes. This results in different κ increase at different sample locations, along with different structure improvement. To relate the intrinsic correlation between κ increase and annealing temperature, we conduct further analysis to determine the annealing temperature at the middle point of the sample and the local κ and study their correlation. The annealing temperature is the highest at center of the sample, resulting in the maximum κ at the center, which is designated as κ_c. Since the temperature at two ends changes very little during the annealing process, the κ at the two ends is set as the κ of as-prepared sample (κ_0). For calculating the κ distribution along CNC, we assumed the κ is linearly distributed along CNCs as $\kappa = \kappa_0 + (\kappa_c - \kappa_0) \times 2x/L$ (x: the distance from the center of the sample). A finite difference method (FDM) was employed to simulate the resistance evolution curve during TET characterization. The length of CNC was divided into 1000 grids. By varying the κ of the center point, we obtain different normalized temperature evolutions during TET measurement. The value giving the best fitting of the experimental data is taken as the value of κ_c.

On the basis of obtained κ_c, the temperature of the center point (T_c) is evaluated from the steady-state heat conduction model during annealing. In this model, thermal transport is independent of ρc_p. For TET characterization at RT, the effect of thermal radiation is negligible [35]. For the annealing process at high temperatures, the thermal radiation becomes a more and more important factor for thermal transport. The emissivity of CNCs at RT is set as 0.85, and it deviates from 0.85 with increased temperature. We found that when the emissivity changes by $\pm 10\%$, the obtained T_c shows a 2% variation. [44] Therefore, the emissivity is set as 0.85 for the whole temperature range in annealing modeling.

Fig. 5(a) and (b) show the relation between κ_c and T_c of the two samples shown in Fig. 4. The two samples show 2.1-fold and 8.7-fold increase in κ by annealing. CNCs were synthesized at 710 °C in our work. Therefore the samples are expected to have dramatic

structure and properties change after the annealing temperature is well above this point. This is confirmed in Fig. 5(a) and (b). Both of them have a turning point around 1000 K (727 °C). Before 1000 K, the temperature is not high enough for crystallinity improvement to increase κ. From 1200 to 1800 K, κ_c shows a rapid increase. After 1800 K, the increasing rate of κ_c slows down with increased temperature because the improvement of crystallinity becomes more and more saturated for increasing κ. This result provides a direct guidance for choosing appropriate annealing temperatures to improve the κ of CNCs. Fig. 5(c) reveals the linear relation between $1/\kappa_c$ and T_c, which are fitted into $1/\kappa_c = -3.5 \times 10^{-4} \times (T_c - 2143)$ m K/W and $1/\kappa_c = -1.5 \times 10^{-4}(T_c - 2533)$ m K/W for sample 1 and 2 respectively. From the fitting curves, we speculate that when the temperature is higher than 2143 K (2533) K, the κ of sample 1 (sample 2) will no longer increase. Therefore, we call this point the saturated temperature. This correlation offers us a quick method to predict the κ with known annealing temperatures.

The common relationship between T_c and κ_c for CNC samples can be expressed as $1/\kappa_c = A \times (T_0 - T_c)$. We still take κ_c as a linear combination of the κ of sp^2 grains and sp^3 networks, expressed as $\kappa_c = \rho c_p[\gamma_c \alpha_a + (1 - \gamma_c)\alpha_b]$. Then we can obtain the correlation between γ_c and T_c, represented as

$$\gamma_c = \frac{B}{(T_0 - T_C)} - C, \qquad (6)$$

where $B = 1/[A\rho c_p(\alpha_a - \alpha_b)]$ and $C = \alpha_b/(\alpha_a - \alpha_b)$. γ_c is the volume fraction of sp^2 grains, which is proportional to the size of sp^2 grains. Thus, we can use Eq. (6) to describe the size of sp^2 grains in a CNC under different annealing temperatures. Ma et al. have reported the variation of sp^2 grain size probed by Raman spectroscopy for the CNCs annealed in a furnace under different temperatures [29]. The plots are shown Fig. 5(d) (reproduced with permission), which are fitted into:

$$L_a = 1.27 \times 10^5/(3700 - T) - 0.31. \qquad (7)$$

This equation demonstrates that the linear relation between $1/\kappa$ and T comes from the linear relation between $1/L_a$ and T.

3.4. Grain size of CNC: uncovered by residual thermal reffusivity and Raman spectrum

In our previous work, we have employed a new concept called thermal reffusivity (Θ) to address the effect of defect scattering on phonon transport in CNCs. Under the single phonon relaxation time approximation, thermal reffusivity can be expressed as $\Theta = 3/v^2\tau$, where v is phonon velocity, τ the average relaxation time during two consecutive scatterings. $v\tau$ corresponds to the mean
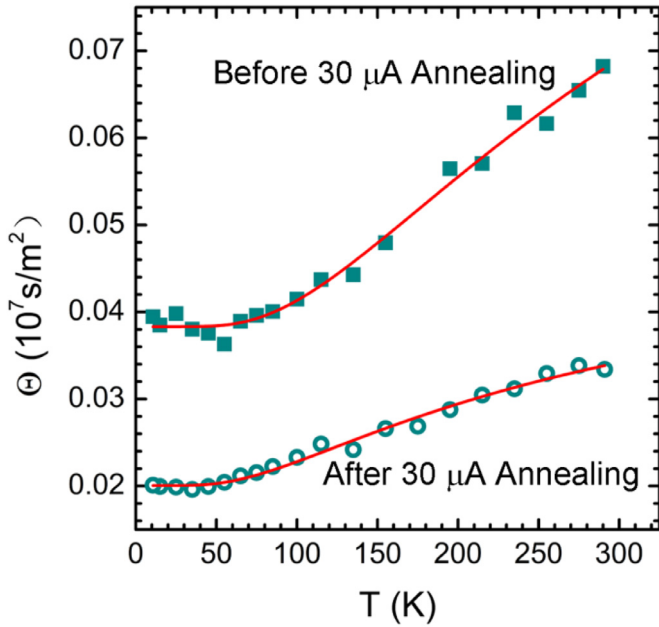
Fig. 6. Thermal reffusivity-temperature curve of a CNC sample before and after 30 μA annealing along with the fitting (red curve) using Eq. (9).

free path (MFP) of phonons. According to the Matthiessen's rule, it is always a good approximation to linearly add all scattering events together, expressed as

$$\frac{1}{\tau} = \frac{1}{\tau_U} + \frac{1}{\tau_D},\tag{8}$$

where τ_U and τ_D correspond to the relaxation times determined by Umklapp scattering and defect scattering. τ_U shows exponential variation with temperature, while τ_D is only determined by microstructure of materials. Excluding the effect of τ_U, it is possible for us to evaluate the defect level of a material. Consequently, the model of thermal reffusivity based on phonon scattering can be expressed as [14]

$$\Theta = \Theta_0 + A \exp(-\theta_D/2T),\tag{9}$$

where Θ_0 is the residual thermal reffusivity at 0 K limit which reflects the defect level. θ_D is Debye temperature.

To investigate the effect of annealing on low temperature thermal behavior, low temperature TET tests from 290 to 10 K for CNC samples before and after annealing were carried out. Fig. 6 shows the thermal reffusivity-temperature curves of another CNC sample before and after 30 μA annealing. The total length and diameter of this sample are 67$\epsilon\mu$m and 371 nm. Using the expression of thermal reffusivity to fit these two curves, the Θ_0 and θ_D before and after 30 μA annealing are calculated to be 3.8 $\times$ 10^5 s/m^2 and 689 K, 2.0 $\times$ 10^5 s/m^2 and 492 K, respectively. After annealing, the residual thermal reffusivity shows a remarkable decrease. From this result, we notice that the CNC sample with better crystallinity after annealing shows a smaller Debye temperature. Debye temperature reflects the interaction among atoms in a lattice. Here, we attribute the Debye temperature reduction to the weakening of interaction of nanograins. More research is needed to look into this problem to uncover the underlying physics.

Excluding the effect of phonon-phonon scattering, MFP for phonon transport at 0 K limit (l_d) is always quite close to the real grain size of CNCs, and can be calculated as $l_d = 3/\Theta_0 v$. Taking 4300 m/s as the value of v, which is taken from that of pyrolytic graphite [45], l_d of the CNC sample before and after annealing is calculated to be 1.8 and 3.5 nm. It shows almost 100% increase, resulting in an increase of RT α by 104%. Here the calculated l_d is
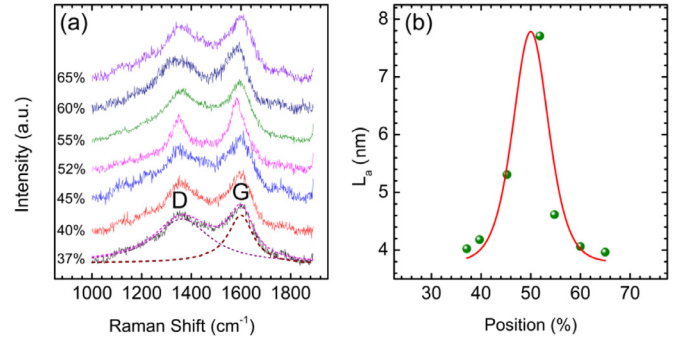

Fig. 7. (a) Raman spectrum of a CNC sample at different positions after being annealed at 30 μA. (b) Extracted grain size from Raman spectrum at different positions of the CNC sample.

an average value along the coil axial direction since the sample is annealed nonuniformly.

Due to nonuniform annealing, the graphite degree varies along the axial direction of the CNC sample. The structural change of annealed CNC was probed by Raman spectroscopy with 532 nm excitation laser. After annealing in vacuum, a single CNC sample was cut at the connection point, and was placed onto silver paste to enhance the Raman signal significantly. Silver particles in the silver paste were used as the enhancing substrate, while the Raman signal of suspended CNC was too weak to be detected.

Fig. 7(a) shows the Raman spectrum at different positions along the length direction of another CNC sample after annealing at 30 μA. The value of positions means the relative distance (the ratio of real distance to sample length) of the measured point to one end of the CNC sample. The G peak around 1581 cm^{-1} and D peak around 1355 cm^{-1} are two characteristic peaks of graphitic materials, representing the in-plane bond stretching motion of sp^2 atoms and the breathing mode of 6-fold aromatic rings occurring when disorders exist. The ratio of D to G peaks (I_D/I_G) is used to calculate the graphite grain size (L_a) by an empirical formula, expressed as $I_D/I_G = C(\lambda)/L_a$, where $C(\lambda) = -12.6 + 0.033\lambda$ [46].λ is the wavelength of excitation laser. The calculated L_a at different positions along the length direction of the CNC sample are shown in Fig. 7(b). L_a shows a sharp increase from 4.0 to 7.8 nm around the center point within $\pm$10% length range (from 40% to 60%). CNCs were synthesized at 710 °C in our work. Thus, the temperature must be higher than 710 °C to achieve annealing. Under 30 μA current annealing, the temperature of the center point is around 1900 K based on our calculation. From the work of Ma et al. [29], it is found that the average grain sizes of CNCs at RT and annealed at 1900 K are 4.1 and 7.2 nm respectively, which are very close to the results in this research. From Fig. 7(b), it is found that only 30% length part of the CNC is effectively annealed to have dramatic grain size increase. The rest 70% part of the sample may experience an improvement of arrangement for graphite nanograins rather than size increasing.

4. Conclusion

Combining TET characterization and Joule heating annealing, in situ investigation of annealing effect on the thermal and electrical properties of CNCs was achieved for the first time. After being annealed at 5–35 μA, the average RT α and σ showed 50%–160% and 100%–170% increase. The reaction/annealing rate against the annealing power has a normal distribution, proposing a normal distribution of the structure activation energy in CNCs. Interestingly, α and σ exhibited excellent linear correlation, which are caused by the barriers of electrons and phonons when they transport between grains. It is found that in the annealing temperature

range of 1200–1800 K, the κ of CNCs showed a rapid improvement, which reached a maximum change up to 8.7-fold. Low temperature tests revealed a 1-fold increase of average grain size and a 197 K decrease of Debye temperature of CNC by annealing. Our residual thermal reffusivity uncovered a dramatic grain size increase from 1.8 nm to 3.5 nm after 30 μA annealing. Our Raman characterization quantified the nonuniform annealing level in the length direction of a CNC sample and uncovered a rapid in situ increase of grain size from 4.0 to 7.8 nm near the middle point. This research illustrates the structural specificity of CNCs a step further and provides crucial guidance for structure manipulation to improve the thermophysical properties of CNCs.

Declaration of Competing Interest

All authors have no competing interests to declare.

CRediT authorship contribution statement

Chenghao Deng: Conceptualization, Methodology, Investigation, Writing - original draft. **Tianze Cong:** Investigation. **Yangsu Xie:** Formal analysis. **Ridong Wang:** Investigation. **Tianyu Wang:** Investigation. **Lujun Pan:** Investigation, Resources. **Xinwei Wang:** Conceptualization, Methodology, Investigation, Writing - review & editing, Supervision, Project administration, Funding acquisition.

Acknowledgements

References

[1] L. Yu, G. Wan, Y. Qin, G. Wang, Atomic layer deposition assisted fabrication of high-purity carbon nanocoil for electrochemical energy storage, Electrochim. Acta 268 (2018) 283–294.

[2] J. Wu, Q. Shi, Z. Zhang, H.H. Wu, C. Wang, F. Ning, S. Xiao, J. He, Z. Zhang, Nature-inspired entwined coiled carbon mechanical metamaterials: molecular dynamics simulations, Nanoscale 10 (2018) 15641–15653.

[3] Y. Nakamura, Y. Suda, R. Kunimoto, T. Iida, H. Takikawa, H. Ue, H. Shima, Precise measurement of single carbon nanocoils using focused ion beam technique, Appl. Phys. Lett. 108 (2016) 153108.

[4] J. Sun, A.A. Koós, F. Dillon, K. Jurkschat, M.R. Castell, N. Grobert, Synthesis of carbon nanocoil forests on BaSrTiO3 substrates with the aid of a Sn catalyst, Carbon N Y 60 (2013) 5–15.

[5] H. Zhan, G. Zhang, C. Yang, Y. Gu, Graphene helicoid: distinct properties promote application of graphene related materials in thermal management, J. Phys. Chem. C 122 (2018) 7605–7612.

[6] X. Han, F. Xu, S. Duan, H. Zhan, Y. Gu, G. Liu, A novel super-elastic carbon nanofiber with cup-stacked carbon nanocones and a screw dislocation, Carbon N Y 154 (2019) 98–107.

[7] X.Q. Chen, S.L. Zhang, D.A. Dikin, W.Q. Ding, R.S. Ruoff, L.J. Pan, Y. Nakayama, Mechanics of a carbon nanocoil, Nano. Lett. 3 (2003) 1299–1304.

[8] L.Z. Liu, H.L. Gao, J.J. Zhao, J.P. Lu, Superelasticity of carbon nanocoils from atomistic quantum simulations, Nanoscale Res. Lett. 5 (2010) 478–483.

[9] R. Cui, L. Pan, D. Zhang, H. Nasir, Electromagnetic microwave absorption properties of carbon nanocoils/tissue, Diam. Relat. Mater 77 (2017) 53–56.

[10] G.H. Kang, S.H. Kim, Effect of incorporating carbon nanocoils on the efficiency of electromagnetic-wave shielding of carbon-nanomaterial composites, Appl. Surf. Sci. 380 (2016) 114–118.

[11] C. Deng, L. Pan, D. Zhang, C. Li, H. Nasir, A super stretchable and sensitive strain sensor based on a carbon nanocoil network fabricated by a simple peeling-off approach, Nanoscale 9 (2017) 16404–16411.

[12] C. Li, L. Pan, C. Deng, T. Cong, P. Yin, Z. Wu, A highly sensitive, wide range pressure sensor based on carbon nanocoil network fabricated by electrophoretic method, J. Mater. Chem. C 5 (2017) 11892–11900.

[13] C. Li, L. Pan, C. Deng, P. Wang, Y. Huang, H. Nasir, A flexible, ultra-sensitive strain sensor based on carbon nanocoil network fabricated by an electrophoretic method, Nanoscale 9 (2017) 9872–9878.

[14] Y. Xie, Z. Xu, S. Xu, Z. Cheng, N. Hashemi, C. Deng, X. Wang, The defect level and ideal thermal conductivity of graphene uncovered by residual thermal reffusivity at the 0 K limit, Nanoscale 7 (2015) 10101–10110.

[15] H. Ma, X. Zhang, R. Cui, F. Liu, M. Wang, C. Huang, J. Hou, G. Wang, Y. Wei, K. Jiang, Photo-driven nanoactuators based on carbon nanocoils and vanadium dioxide bimorphs, Nanoscale 10 (2018) 11158–11164.

[16] A. Volodin, D. Buntinx, M. Ahlskog, A. Fonseca, J.B. Nagy, C. Van Haesendonck, Coiled carbon nanotubes as self-sensing mechanical resonators, Nano. Lett. 4 (2004) 1775–1779.

[17] L. Pan, T. Hayashida, M. Zhang, Y. Nakayama, Field emission properties of carbon tubule nanocoils, Jpn. J. Appl. Phys. 40 (2001) L235–L237.

[18] K.J. Chung, N.W. Pu, M.J. Youh, Y.M. Liu, M.D. Ger, K. Cheng, J.C. Jiang, Improvement of field-emission-lamp characteristics using nitrogen-doped carbon nanocoils, Diam. Relat. Mater. 53 (2015) 1–10.

[19] W.H. Choi, J.C. Mi, H.B. Jin, Nitrogen-doped carbon nanocoil array integrated on carbon nanofiber paper for supercapacitor electrodes, ACS Appl. Mater. Interf. 7 (2015) 19370–19381.

[20] L. Wang, Z. Liu, Q. Guo, G. Wang, J. Yang, P. Li, X. Wang, L. Liu, Electrochemical properties of carbon nanocoils and hollow graphite fibers as anodes for rechargeable lithium ion batteries, Electrochim. Acta 199 (2016) 204–209.

[21] A. Ludwig, K.J. Webb, H. Ågren, Magnetism from carbon nanocoil mixtures, J. Appl. Phys. 118 (2015) 2075–2223.

[22] U. Eguchi, H. Takikawa, Y. Suda, Electromagnetic wave absorption characteristics of multiwalled carbon nanocoils, Jpn. J. Appl. Phys. 53 (2014) 205–211.

[23] S. Zhao, Z. Gao, C. Chen, G. Wang, B. Zhang, Y. Chen, J. Zhang, X. Li, Y. Qin, Alternate nonmagnetic and magnetic multilayer nanofilms deposited on carbon nanocoils by atomic layer deposition to tune microwave absorption property, Carbon N Y 98 (2016) 196–203.

[24] C. Deng, L. Pan, C. Li, X. Fu, R. Cui, H. Nasir, Helical gold nanotube film as stretchable micro/nanoscale strain sensor, J. Mater. Sci. 53 (2017) 1–12.

[25] Y.M. Sun, C.W. Wang, L.J. Pan, X. Fu, P.H. Yin, H.L. Zou, Electrical conductivity of single polycrystalline-amorphous carbon nanocoils, Carbon N Y 98 (2016) 285–290.

[26] H.S. Chiu, P.I. Lin, H.C. Wu, W.H. Hsieh, C.D. Chen, Y.T. Chen, Electron hopping conduction in highly disordered carbon coils, Carbon N Y 47 (2009) 1761–1769.

[27] N. Tang, W. Kuo, C. Jeng, L. Wang, K. Lin, Y. Du, Coil-in-coil carbon nanocoils: 11 g-scale synthesis, single nanocoil electrical properties, and electrical contact improvement, ACS Nano. 4 (2010) 781–788.

[28] C. Deng, L. Pan, H. Ma, R. Cui, Electromechanical vibration of carbon nanocoils, Carbon N Y 81 (2015) 758–766.

[29] H. Ma, K. Nakata, L.J. Pan, K. Hirahara, Y. Nakayama, Relationship between the structure of carbon nanocoils and their electrical property, Carbon N Y 73 (2014) 71–77.

[30] S. Ihara, S. Itoh, J. Kitakami, Helically coiled cage forms of graphitic carbon, Phys. Rev. B 48 (1993) 5643–5647.

[31] N.J. Tang, Y. Yang, K.J. Lin, W. Zhong, C.T. Au, Y.W. Du, Synthesis of plait-like carbon nanocoils in ultrahigh yield, and their microwave absorption properties, J. Phys. Chem. C 112 (2008) 10061–10067.

[32] S. Dohn, K. Mølhave, P. Bøggild, Direct measurement of resistance of multi-walled carbon nanotubes using micro four-point probes, Sensor Lett. 3 (2005) 300–303.

[33] P.R. Goggin, W.N. Reynods, The elastic constants of reactor graphites, Philos. Mag. 16 (1967) 14.

[34] K. Hirahara, K. Nakata, Y. Nakayama, Non-linear annealing effect on correlation between crystallinity and oscillation of carbon nanocoils, Mater. Sci. Eng. A 595 (2014) 205–212.

[35] C. Deng, Y. Sun, L. Pan, T. Wang, Y. Xie, L. Jing, B. Zhu, X. Wang, Thermal diffusivity of single carbon nanocoil: uncovering the correlation with temperature and domain size, ACS Nano. 10 (2016) 9710–9719.

[36] H. Ma, L. Pan, Q. Zhao, Z. Zhao, J. Qiu, Thermal conductivity of a single carbon nanocoil measured by field-emission induced thermal radiation, Carbon N Y 50 (2012) 778–783.

[37] R. Cui, L. Pan, C. Deng, Synthesis of carbon nanocoils on substrates made of plant fibers, Carbon N Y 89 (2015) 47–52.

[38] J.Q. Guo, X.W. Wang, T. Wang, Thermal characterization of microscale conductive and nonconductive wires using transient electrothermal technique, J. Appl. Phys. 101 (2007) 063537.

[39] J. Hou, X. Wang, P. Vellelacheruvu, J. Guo, L. Chang, H.M. Cheng, Thermal characterization of single-wall carbon nanotube bundles using the self-heating 3ω technique, J. Appl. Phys. 100 (2006) 971 -125.

[40] J. Guo, X. Wang, T. Wang, Thermal characterization of microscale conductive and nonconductive wires using transient electrothermal technique, J. Appl. Phys. 101 (2007) 2996 -125.

[41] A.J. Bullen, K.E. Ohara, D.G. Cahill, A. Monteiro, A. Von Keudell, Thermal conductivity of amorphous carbon thin films, J. Appl. Phys. 88 (2000) 6317–6320.

[42] R. Wang, H. Zobeiri, H. Lin, W. Qu, X. Bai, C. Deng, X. Wang, Anisotropic thermal conductivities and structure in lignin-based microscale carbon fibers, Carbon N Y 147 (2019) 58–69.

[43] M. Shamsa, W.L. Liu, A.A. Balandin, C. Casiraghi, W.I. Milne, A.C. Ferrari, Thermal conductivity of diamond-like carbon films, Appl. Phys. Lett. 89 (2006) 085401.

[44] J. Liu, W. Qu, Y. Xie, B. Zhu, T. Wang, X. Bai, X. Wang, Thermal conductivity and annealing effect on structure of lignin-based microscale carbon fibers, Carbon N Y 121 (2017) 35–47.

[45] G.A. Slack, Anisotropic thermal conductivity of pyrolytic graphite, Phys. Rev. 127 (1962) 694–701.

[46] A.C. Ferrari, J. Robertson, Interpretation of Raman spectra of disordered and amorphous carbon, Phys. Rev. B Cond. Matt. 61 (2000) 14095–14107.